

## ACTIVE GALACTIC NUCLEI WITH DOUBLE-PEAKED NARROW LINES: ARE THEY DUAL AGNS?

JIAN-MIN WANG<sup>1,2</sup>, YAN-MEI CHEN<sup>1,3</sup>, CHEN HU<sup>1</sup>, WEI-MING MAO<sup>4</sup>,  
SHU ZHANG<sup>1</sup> AND WEI-HAO BIAN<sup>5</sup>

Received 2009 July 27; accepted 2009 September 30

### ABSTRACT

Double-peaked [O III] profiles in active galactic nuclei (AGNs) may provide evidence for the existence of dual AGNs, but a good diagnostic for selecting them is currently lacking. Starting from  $\sim 7000$  active galaxies in SDSS DR7, we assemble a sample of 87 type 2 AGNs with double-peaked [O III] profiles. The nuclear obscuration in the type 2 AGNs allows us to determine redshifts of host galaxies through stellar absorption lines. We typically find that one peak is redshifted and another is blueshifted relative to the host galaxy. We find a strong correlation between the ratios of the shifts and the double peak fluxes. The correlation can be naturally explained by the Keplerian relation predicted by models of co-rotating dual AGNs. The current sample statistically favors that most of the [O III] double-peaked sources are dual AGNs and disfavors other explanations, such as rotating disk and outflows. These dual AGNs have a separation distance at  $\sim 1$  kpc scale, showing an intermediate phase of merging systems. The appearance of dual AGNs is about  $\sim 10^{-2}$ , impacting on the current observational deficit of binary supermassive black holes with a probability of  $\sim 10^{-4}$  (Boroson & Lauer).

*Subject headings:* black hole physics — galaxies: evolution

### 1. INTRODUCTION

Supermassive black hole binaries and dual AGNs are the natural result of the current  $\Lambda$ CDM cosmological paradigm, in which galaxies grow hierarchically through minor or major mergers. However, evidence for such systems is elusive and confirmed cases are rare despite circumstantial evidence. Examples can be found in Kochanek et al. (1999), Junkkarinen et al. (2001), Ballo et al. (2004), Maness et al. (2004), Guainazzi et al. (2005), Rodriguez et al. (2006), Hudson et al. (2006), Barth et al. (2008). The best-known examples of dual AGNs are found in NGC 6240 (Komossa et al. 2003), EGSD2 J142033+525917 (Gerke et al. 2007), EGSD2 J141550+520929 (Comerford et al. 2009a), the  $z = 0.36$  galaxy COSMOS J100043+020637 (Comerford et al. 2009b). Ideally, analysis of a large statistical sample should be undertaken.

The narrow emission lines in AGNs are generally thought to be produced by clouds in the narrow line regions at a scale of  $\sim 1$  kpc, where they are photoionized by the central energy source (e.g. Netzer et al. 2006). It is common that the [O III]  $\lambda 5007$  line has an asymmetric blue wing (Boroson 2005, Komossa et al. 2008), which could be caused by winds and outflows. On the other hand, about 1% AGNs have double-peaked [O III] profiles. The origin of the double-peaked emission lines remains unclear, but they have been interpreted as evidence for bi-polar outflows in the early 1980s (Heckman et al. 1981, 1984; Whittle 1985a,b,c) or disk-shaped narrow line regions (Greene et al. 2005). Evidence based on objects mentioned above suggests dual AGNs as an alternative explanation of the double-peaked profiles. However, more robust observational evidence is needed.

In this Letter, we select type 2 AGNs from SDSS DR7. The obscuration of the nucleus in these sources allows us to deter-

mine the redshifts of the host galaxies through the stellar absorption lines and investigate the properties of the double peaks. We find a strong correlation between the ratios of the shifts and the double peak fluxes. This is most naturally explained by the Keplerian relation of co-rotating dual AGNs.

### 2. SAMPLE AND DATA ANALYSIS

#### 2.1. Sample selection

We start from the galaxy sample of SDSS DR7 and select active galaxies based on the widely used BPT diagram (Baldwin et al. 1981). Using the measured fluxes of narrow emission lines from the MPA/JHU catalog<sup>6</sup>, we separate type 2 AGNs from other sources according to their line ratios:  $\log([\text{O III}]/\text{H}\beta) > 0.61 / \{\log([\text{N II}]/\text{H}\alpha) - 0.47\} + 1.19$  (the solid curve in Fig. 2 from Kewley et al. 2001), or  $\log([\text{N II}]/\text{H}\alpha) > 0.47$ . We select those objects with SDSS  $r$ -band magnitude  $r < 17.7$ , redshift  $z \leq 0.15$  and equivalent width of [O III]  $\lambda 5007$  greater than 5. In total, 6780 type 2 AGNs follow from this criterion. We use stellar population synthesis models to separate the spectra of the host galaxies (Tremonti et al. 2004) from those of the AGNs. The redshifts of the host galaxies are re-measured through the absorption lines (see §2.2 for details). [O III]  $\lambda 5007$  is fitted by two Gaussian profiles in order to select the double-peaked AGNs. Those sources having two [O III]  $\lambda 5007$  components (one blueshifted and one redshifted, relative to the host galaxies) separated by  $\Delta\lambda \geq 1$  (based on the redshift accuracy, see §2.2) and a flux ratio in the range of  $\sim [0.1, 10]$ , are selected. This results in 286 candidates. We visually inspect their spectra and remove those galaxies with a false component. For these galaxies which have very large or small flux ratios, the double-peaked profiles are not convincing. Finally, we are left with 87 sources having a flux ratio in the range of  $[0.3, 3]$ , 44

<sup>1</sup> Key Laboratory for Particle Astrophysics, Institute of High Energy Physics, Chinese Academy of Sciences, 19B Yuquan Road, Beijing 100049, China

<sup>2</sup> Theoretical Physics Center for Science Facilities, Chinese Academy of Sciences, China

<sup>3</sup> Graduate University of Chinese Academy of Sciences, 19A Yuquan Road, Beijing 100049, China

<sup>4</sup> National Astronomical Observatories, Chinese Academy of Sciences, 20 Datun Road, Beijing 100020, China

<sup>5</sup> Physics Department and Institute of Theoretical Physics, Nanjing Normal University, Nanjing 210097, China

<sup>6</sup> The MPA/JHU catalog can be downloaded from <http://www.mpa-garching.mpg.de/SDSS/DR7>.

of which have high enough S/N of the spectra to see similar double-peaked structures in other lines (e.g. [O III]  $\lambda$ 4959, H $\beta$ , H $\alpha$ , [N II], [S II]). Fig. 1 shows one example.

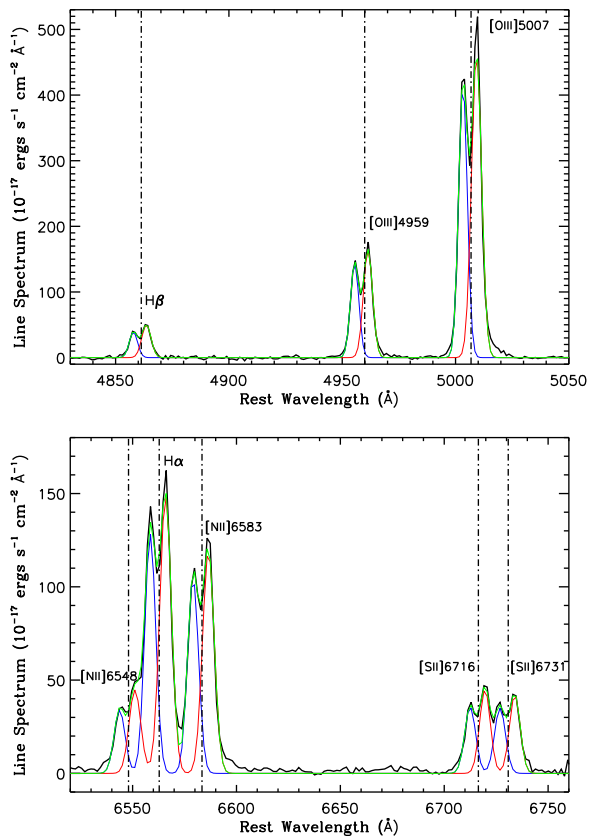


FIG. 1.— Spectra of object SDSS J080218.65+304622.8 selected from our sample. Blue lines are the blue-shifted components, and red lines are the red-shifted components. The green line represents the final fit. It is generally found that the separation ratios of the two components of H $\beta$ , H $\alpha$ , [N II], [S II] are roughly equal to that of [O III]. This indicates that the source is a candidate for a dual AGN.

## 2.2. Determinations of galaxy redshifts

One key parameter in this work is the ratio of wavelength shifts of the two components relative to the host galaxy. This ratio is sensitive to the host galaxy redshift. In order to get a robust shift ratio, a host galaxy redshift accuracy of  $\Delta z/z = \Delta\lambda/\lambda \sim 2 \times 10^{-4}$  is required based on the redshift range of our sample and 1 Å separation limit in term of SDSS spectral resolution. We first fit the galaxy spectrum by a stellar population model (Tremonti et al. 2004), under the basic assumption that any galaxy star formation history can be approximated by a sum of discrete bursts. The library of template spectra is composed of single stellar population models generated using the population synthesis code of BC03 (Bruzual & Charlot 2003), including models of ten different ages (0.005, 0.025, 0.1, 0.2, 0.6, 0.9, 1.4, 2.5, 5, 10 Gyrs) and four metallicities (0.004, 0.008, 0.017, 0.05). The template spectra are convolved to the stellar velocity dispersion measured for each SDSS galaxy, and four best fitting model spectra with fixed metallicity are constructed from a non-negative linear combination of the template spectra, with dust attenuation modeled as an additional free parameter. The results of the stellar population synthesis can be found from the SDSS-MPA webpage. We use the redshift given by SDSS

pipeline as initial value for our iterative fitting technique. The absorption line redshift is determined by the fit having the lowest  $\chi^2$  value. The uncertainty of the redshift is given by the width of the  $\chi^2$  minimum at which  $\Delta\chi^2 = 1$ . We give the redshifts of the host galaxies, the blue and redshifts of the two components of narrow emission lines and their corresponding fluxes in Table 1, respectively.

## 3. PROPERTIES OF THE DOUBLE-PEAKED LINES

### 3.1. The two components in the BPT diagram

The location of AGNs in the BPT diagram is mainly determined by the SED of the photoionizing central engine. Since SEDs are strongly controlled by the Eddington ratios (Wang et al. 2004; Shemmer et al. 2006; Yang, et al. 2007; Gu & Cao 2009), the separation of the two components ( $\mathcal{D}$ ) in the BPT diagram provides quantitative information on the degree of similarity between the Eddington ratios of accreting black holes.

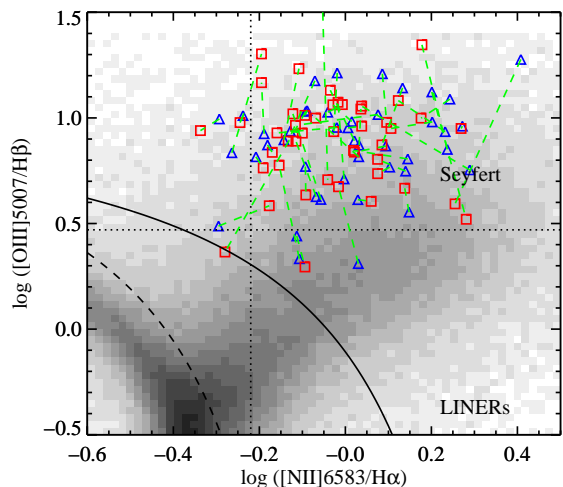


FIG. 2.— The BPT diagram of each of the two components. The solid and dashed lines correspond to the dividing lines between AGN and star forming galaxies of Kewley et al. (2001) and Kauffmann et al. (2003), respectively. Seyfert galaxies are often defined to have [O III]  $\lambda$ 5007/H $\beta$  > 3 (horizontal dotted line) and [N II]  $\lambda$ 6583/H $\alpha$  > 0.6 (vertical dotted line), and LINERs to have [O III]  $\lambda$ 5007/H $\beta$  < 3 and [N II]  $\lambda$ 6583/H $\alpha$  < 0.6. Blue triangles indicate the blue-shifted components whereas the red squares indicate the redshifted ones. The two components belonging to a single source are linked by dashed green lines. The double-peaked components in each object are very similar in most of the sample, indicating that the two components are produced by similar illuminating sources. Overplotted is the general population of SDSS DR7 galaxies.

We examine the locations of the two components in the BPT diagram in order to explore their central engines. There are 44 objects in our sample with clear double-peaked structure in H $\beta$ , [O III]  $\lambda$ 5007, H $\alpha$  and [N II]  $\lambda$ 6583. Fig. 2 shows the two components in the BPT diagram for the 44 AGNs. The solid and dashed lines correspond to the dividing lines between AGN and star forming galaxies of Kewley et al. (2001) and Kauffmann et al. (2003), respectively. The entire sample of SDSS DR7 galaxies is overplotted for comparison. Blue triangles indicate the blue-shifted components, while red squares indicate the red-shifted components. Green dashed lines link the two components in each object. From Fig. 2, we can learn that each component of all the 44 objects are located in the Seyfert regime. The  $\mathcal{D}$ -distribution is peaked around zero from Fig. 3, rather than flat. The mean value of  $\mathcal{D}$  is about 0.23. This shows that for each source, the two components have similar Eddington ratios.

We would like to point out that it is beyond the scope of the present paper to investigate the qualitative relation between  $\mathcal{D}$  and the degree of similarity between the two emitters. However it is robust that the smaller the  $\mathcal{D}$ , the more similar the two emitters are. We have to note that no object has  $\mathcal{D} = 0$ , which could mean that the two narrow line regions share same or one illuminating source.

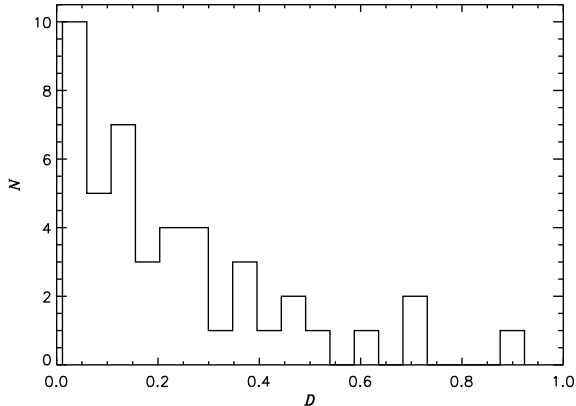


FIG. 3.— The  $\mathcal{D}$ -distribution. The sources peak around zero. The mean value  $\langle \mathcal{D} \rangle \approx 0.23$ . This implies that the two components have similar photoionizing energy sources.

### 3.2. A correlation between the line shifts and the luminosities

In order to further study the properties of the double-peaked [O III]  $\lambda 5007$  and its origin, we measure the shifts  $\Delta\lambda_1 = |\lambda_1 - \lambda_0|$  and  $\Delta\lambda_2 = |\lambda_2 - \lambda_0|$ , where  $\lambda_1$  and  $\lambda_2$  are the peak wavelength of the blue and red components of [O III]  $\lambda 5007$  in the rest frame of the host galaxies, respectively, and  $\lambda_0 = 5006.84\text{\AA}$ , and their corresponding  $L_{[\text{O III}],1}$  and  $L_{[\text{O III}],2}$  are the corresponding luminosities of the blue and red components. We define  $\Delta\lambda_1/\Delta\lambda_2$  and  $L_{[\text{O III}],1}/L_{[\text{O III}],2}$  as the ratios of the shifts and double peak fluxes, respectively. Fig. 4 shows a striking correlation between  $\Delta\lambda_1/\Delta\lambda_2$  and  $L_{[\text{O III}],1}/L_{[\text{O III],2}$  which we fit as

$$\log\left(\frac{L_{[\text{O III}],1}}{L_{[\text{O III],2}}}\right) = (0.005 \pm 0.010) - (0.960 \pm 0.11) \log\left(\frac{\Delta\lambda_1}{\Delta\lambda_2}\right), \quad (1)$$

with the Pearson correlation coefficient of  $-0.43$  and a chance probability of  $3 \times 10^{-5}$ . We would like to stress here that this correlation poses a strong constraint on the origin of the double peaks since it establishes a physical relation between the two components. In the following section, we discuss the possible origin of the double-peaked line structure according to this correlation.

## 4. DISCUSSION

The origin of double-peaked Balmer broad lines in quasars is likely ascribed to the outer part of the accretion disk surrounding an SMBH (Eracleous et al. 2003), but only one potential exception from 17500 SDSS DR5 quasars (Boroson & Lauer 2009). The size of narrow line regions scales with [O III]  $\lambda 5007$  luminosity as  $R_{\text{NLR}} = 1.2L_{[\text{O III],42}}^{0.5}$  kpc, where  $L_{[\text{O III],42}} = L_{[\text{O III}]} / 10^{42} \text{ erg s}^{-1}$  (Netzer et al. 2006). Double-peaked narrow emission lines of active galaxies are plausibly caused by two orbiting narrow line regions of dual AGNs during an ongoing merger of their host galaxies (Bogdanovic et al. 2008), but it is difficult to distinguish such a configuration from the occasional projections of quasars, gravitational lensing effects (Mortlock et al. 1999; Kochanek et al. 1999), disks, bi-

polar outflows and jet/cloud interactions (Heckman et al. 2009). We first consider the scenario of dual AGNs as explanation of the strong correlation found in §3.2.

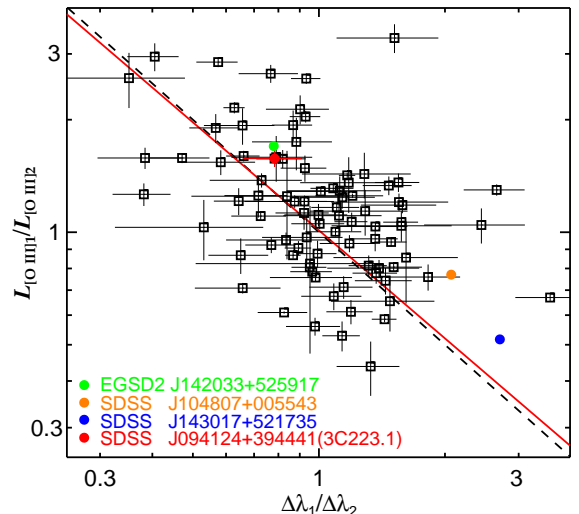


FIG. 4.— Correlation between the flux and shift ratios of the two [O III]  $\lambda 5007$  components. Black squares represent our sample. The red solid line is the best-fit linear correlation given in eq. (1). The dashed line is eq. (5) by setting  $\epsilon_{1,2} = 1$ . We find that the Keplerian relation matches the observed correlation very well. The object SDSS J104807+005543 is from Zhou et al. (2005). Overplotted circles are four dual AGNs known from published literature.

### 4.1. Kepler diagram

The process of merging of two galaxies can be divided into three phases (Begelman et al. 1980). At the time of merging, the bulges are homogenized within the friction timescale, but the narrow line regions are still bounded to their original host systems. Galaxies in this stage are the most plausible sites for hosting dual SMBHs and are expected to exhibit double nuclei in the optical and infrared. Since the [O III]  $\lambda 5007$  emission is the most powerful narrow line, we will mainly use this line in the Kepler diagram.

According to Kepler's law, for a binary system with the components  $M_1$  and  $M_2$ , the orbital velocity ratio of the two components is given by

$$\frac{V_1}{V_2} = \frac{M_2}{M_1}, \quad (2)$$

if the total angular momentum is conserved for the circular orbital system. An emission line with rest wavelength  $\lambda_0$  will split into red and blue components due to the orbital rotation around the mass center, and we have

$$\frac{V_1}{V_2} = \frac{\Delta\lambda_1}{\Delta\lambda_2}, \quad (3)$$

where blue- and redshifts are measured by  $\Delta\lambda_1 = |\lambda_1 - \lambda_0|$  and  $\Delta\lambda_2 = |\lambda_2 - \lambda_0|$ ,  $\lambda_1$  and  $\lambda_2$  are the wavelengths at the rest frame of the host galaxies.

The masses of the two components are difficult to measure directly, but their ratio can be reasonably estimated from the [O III]  $\lambda 5007$  luminosity. For a binary system with large separation, the potential of the two components will include mass of the bulges. However, the mass ratio should be equal to the SMBH ratio provided the Magorrian relation holds (Magorrian et al. 1998; Marconi & Hunt 2003). We have  $M_{\bullet,1}(M_{\bullet,2}) \propto M_1(M_2)$ , where  $M_{\bullet,1}$  and  $M_{\bullet,2}$  are the masses of the SMBH components corresponding to the two progenitor galaxies. If

we measure the luminosities of the blue and red components of the [O III]  $\lambda 5007$  line, we have

$$\frac{M_{\bullet,2}}{M_{\bullet,1}} = \epsilon_{1,2} \frac{L_{[\text{O III}],2}}{L_{[\text{O III}],1}}, \quad (4)$$

where  $\epsilon_{1,2} = \epsilon_1/\epsilon_2$ ,  $\epsilon_1$  and  $\epsilon_2$  are the Eddington ratios of the two SMBHs (the bolometric luminosity is obtained from  $L_{\text{Bol}} = \mathcal{C}L_{[\text{O III}]}$   $= \epsilon L_{\text{Edd}}$ .  $\mathcal{C}$  is a bolometric correction factor from the [O III] luminosity). The dynamical criterion for having dual AGNs is then given by

$$\frac{L_{[\text{O III}],1}}{L_{[\text{O III}],2}} = \epsilon_{1,2} \frac{\Delta\lambda_2}{\Delta\lambda_1}. \quad (5)$$

In principle,  $\epsilon_{1,2}$  is unknown observationally. Interestingly, the flux ratio range of the sample corresponds to the major merger systems if the double-peaked sources are dual AGNs and each AGN is accreting at similar Eddington ratios. Therefore  $\epsilon_{1,2} \sim 1$  holds for the two SMBHs, which are driven by similar environments of tidal interaction between the two galaxies during major mergers. This is also supported by the correlation from Fig. 4.

Equation (5) has some striking advantages for finding dual AGNs: 1) both sides are easily measured from observed spectra; 2) the equation is independent of the inclinations of the systems. We stress here that equation (5) is a dynamical relation to examine the origin of the double-peaked systems.

In order to understand the implication of the correlation observed (eq. 1), we need to compare it with eq. (5). We find that the correlation (eq. 1) agrees well with eq. (5) if  $\epsilon_{1,2} \sim 1$  in case of  $\mathcal{D} \sim 0$ . The correlation lends strong support for the scenario of dual AGNs in our sample. We thus have  $\sim 90$  candidates from  $\sim 7000$  AGNs, and the fraction of dual AGN candidates is about  $f_{\bullet\bullet} \sim 10^{-2}$ . This nicely agrees with the fraction of major mergers in the local universe from observations (Ryan et al. 2008), but is much higher than the presence of binary SMBHs with a probability of  $10^{-4}$  as found by Boroson & Lauer (2009).

According to Kepler's law, we have a separation  $A = 0.48q^2M_{10}(1+q)^{-1}\delta_{-3}^{-2}$  kpc, where the mass ratio  $q = M_2/M_1$ ,  $\delta_{\lambda_1} = |\lambda_1/\lambda_0 - 1|$ , and  $\delta_{-3} = \delta_{\lambda_1}/10^{-3}$  and  $M_{10} = M_1/10^{10}M_{\odot}$  is the mass of the bulge or spheroid. Though the exact masses of the systems are unknown, the separation should be typically less than 1 kpc (smaller than 1.4 kpc in NGC 6240, Komossa et al. 2003). A visual inspection of our candidates shows they most often have structures of tidal tails, that can be related to major mergers. They thus likely contain two black holes as suggested by numerical simulations.

The uncertainties in eq. (5) are mainly due to the uncertainties in  $\epsilon_{1,2}$ . The dispersion of the parameter  $\epsilon_{1,2}$  is expressed by  $\sigma(\epsilon_{1,2})/\langle\epsilon_{1,2}\rangle = \sqrt{2}\sigma(\epsilon_1)/\langle\epsilon_1\rangle$ , where  $\langle\rangle$  indicates average values, and we use  $\sigma(\epsilon_1)/\langle\epsilon_1\rangle = \sigma(\epsilon_2)/\langle\epsilon_2\rangle$ . It turns out that  $\sigma(\epsilon_1)/\langle\epsilon_1\rangle \approx 0.3$  based on local AGNs (Greene & Ho 2007), and hence  $\sigma(\epsilon_{1,2})/\langle\epsilon_{1,2}\rangle \approx 0.4$ . It should be noted that the dispersion in  $\epsilon_{1,2}$  is probably a lower limit on the true scatters in the Kepler diagram. Additionally, the actual orbit of dual AGNs could be elliptical rather than a perfect circular, leading to additional scatters in Fig. 4.

#### 4.2. Disfavoring other explanations

Disk or bi-polar outflows are able to produce double-peaked [O III] profiles, and are generally employed to interpret the origin of double peaks (e.g. Eracleous & Halpern 2003; Heckman 1981, 1984; Whittle 1985a,b). For bi-polar symmetric

outflows, the observed fluxes of the blue- and redshifted components are  $\mathcal{D}_{\text{blue}}^3 I_0$  and  $\mathcal{D}_{\text{red}}^3 I_0$ , where  $I_0$  is the intrinsic intensity of the emission line at  $\lambda_0$ ,  $\mathcal{D}_{\text{blue}} = 1/\Gamma(1 - \beta \cos \Theta)$  and  $\mathcal{D}_{\text{red}} = 1/\Gamma(1 + \beta \cos \Theta)$  are the Doppler factors of the approaching and receding outflows, respectively,  $\beta = V_{\text{out}}/c$  is the velocity of the outflows,  $\Gamma = 1/(1 - \beta^2)^{1/2}$  is the Lorentz factor and  $\Theta$  is the orientation angle of the outflow with respect to observers (e.g. Rybicki & Lightman 1979). We have the luminosity ratio  $L_{[\text{O III}],1}/L_{[\text{O III}],2} = (1 + \beta \cos \Theta)^3/(1 - \beta \cos \Theta)^3$  whereas the shift ratio  $\Delta\lambda_1/\Delta\lambda_2 = (1 + \beta \cos \Theta)/(1 - \beta \cos \Theta)$ . It is then expected that  $L_{[\text{O III}],1}/L_{[\text{O III}],2} = (\Delta\lambda_1/\Delta\lambda_2)^3$ . This directly conflicts with the correlation discovered from the sample. A similar relation is expected for the disk origin though there is a geometry-dependence of the emission line profiles. Additionally the range of the ratios should be very narrow since the velocities in outflows and disk rotations are much smaller than the light speed. The current correlation does not favor the disk or bi-polar origins of the double peak profiles.

#### 4.3. Additional notes

The object SDSS J094124+394441 in our sample is 3C 223.1, which is a well-known X-shaped radio source (Merritt & Ekers 2002). We mark this object with a red circle in Fig. 4. Additionally, Cheung (2007) provides a list of 100 X-shaped radio objects: 22 of these have SDSS spectra, and one (SDSS J143017+521735) has double-peaked narrow emission lines (see the blue circle in Fig. 4). The two independent confirmations lend more support to that these two objects may be dual AGNs.

If activities of SMBHs are triggered via mergers (Di Matteo et al. 2005), a transition phase of dual AGNs should be common before the formation of the SMBH binaries, which are bounded by the potential of the two black holes (Begelman et al. 1980). X-shaped radio sources have been suggested to be binary black holes (Merritt & Ekers 2002) in light of two double-sided jets. However, the fraction of radio-loud AGNs is  $\sim 10\%$ , meaning that only  $\sim 1\%$  of dual AGNs are expected to be X-shaped in the radio. Such low occurrence makes radio images relatively non-effective in searching for dual AGNs or SMBH binaries, but the double-peaked sources could be identified by radio morphology as a supplementary criterion. Multi-wavelength observations of these sources are important in further verifying their properties.

## 5. CONCLUSIONS

We find a striking correlation between the ratios of [O III] shifts and the double peak fluxes in a sample of 87 AGNs from the SDSS. This correlation strongly favors the explanation of dual AGNs in light of the Kepler diagram and does not favor a disk and outflow origin. The results also show that dual AGNs at 1 kpc scale are common, strongly impacting on the observational deficit of binary SMBHs with a probability of  $\sim 10^{-4}$  as shown by Boroson & Lauer (2009). The present correlation in the Kepler diagram and the dynamical criterion offer an efficient way to select targets (e.g. full version of Table 1) for future image detections in optical band and X-rays.

Finally, redshifts of host galaxies are a vital parameter in determination of the position of sources in the Kepler diagram. Higher resolution spectra are extremely important to diagnose dual AGNs among the weak double-peaked sources. The method presented in this paper is ideal for the study of such sources using high resolution spectra in the future.

We are very grateful to the referee for useful comments and suggestions that have strengthened this work. T. Heckman, G. Kauffmann, C. Tremonti, R. A. Overzier, H. Netzer, T.-G. Wang and L. C. Ho are greatly thanked for useful discussions and comments, especially, C. Tremonti who helped us determine the redshifts of host galaxies. We appreciate the stimulating discussions among the members of the IHEP AGN group. The research is supported by NSFC-10733010 and 10821061,

CAS-KJXC2-YW-T03, and 973 project (2009CB824800).

*A note added.* We were pleased to learn from a talk presented in the KIAA meeting on July 24, 2009 that D. Xu & S. Komossa (see their paper: arXiv:0908.3140) were working on one individual double-peaked object. After we submitted our paper on 27 July, 2009, two more papers have appeared on astro-ph (Smith et al., arXiv:0908.1998; Liu et al., arXiv:0908.2426). These studies are highly complementary in this hot topic.

#### REFERENCES

- Baldwin, J. A., Phillips, M. M. & Terlevich, R. 1981, *PASP*, 93, 5  
 Ballo, L., et al. 2004, *ApJ*, 600, 634  
 Barth, A., J. 2008, *ApJ*, 683, L119  
 Begelman, M., Blandford, R. & Rees, M. J. 1980, *Nature*, 287, 307  
 Bogdanovic, T., Smith, B. D., Sigurdsson, S. & Eracleous, M. 2008, *ApJS*, 174, 455  
 Boroson, T. A. 2005, *AJ*, 130, 381  
 Boroson, T. A. & Lauer, T. R. 2009, *Nature*, 458, 53  
 Bruzual, G. & Charlot, S. 2003, *MNRAS*, 344, 1000  
 Cheung, C. C. 2007, *AJ*, 133, 2097  
 Comerford, J. M. et al. 2009a, *ApJ*, 698, 956  
 Comerford, J. M. et al. 2009b, arXiv:0906.3517  
 Di Matteo, T. et al. 2005, *Nature*, 433, 604  
 Eracleous, M. & Halpern, J. 2003, *ApJ*, 599, 886  
 Gerke, B. F. et al. 2007, *ApJ*, 660, 23.  
 Greene, J. E. & Ho, L. C. 2005, *ApJ*, 627, 721  
 Greene, J. E. & Ho, L. C. 2007, *ApJ*, 667, 131  
 Gu, M. & Cao, X. 2009, *MNRAS* in press, arXiv:0906.3560  
 Guainazzi, M. et al. 2005, *A&A*, 429, 9  
 Heckman, T. M. et al. 1981, *ApJ*, 247, 403  
 Heckman, T. M. et al. 1984, *ApJ*, 281, 525  
 Heckman, T. et al. 2009, *ApJ*, 695, 363  
 Hudson, D. S., et al. 2006, *A&A*, 453, 433  
 Junkkarinen, V. et al. 2001, *ApJ*, 549, L155  
 Kauffmann, G. et al. 2003, *MNRAS*, 346, 1055  
 Kewley, L. J. et al. 2001, *ApJ*, 556, 121  
 Kochanek, C.S., Falco, E.E., and Munoz, J.A. 1999, *ApJ*, 510, 590  
 Komossa, S. et al. 2003, *ApJ*, 582, L15  
 Komossa, S. et al. 2008, *ApJ*, 680, 926  
 Liu, X. et al. 2009, arXiv:0908.2426  
 Magorrian, J. et al. 1998, *AJ*, 115, 2285  
 Maness, H. L. et al. 2004, *ApJ*, 602, 123  
 Marconi, A. & Hunt, L. K. 2003, *ApJ*, 589, L21  
 Merritt, D. & Ekers, E. R. 2002, *Science*, 297, 1310  
 Mortlock, D. J., Webster, R. L. & Francis, P. J. 1999, *MNRAS*, 309, 836  
 Netzer, H. et al. 2006, *A&A*, 453, 525  
 Rodriguez, C. et al. 2006, *ApJ*, 646, 49  
 Ryan, R. E., Jr., Cohen, S. H., Windhorst, R. A., Silk, J. 2008, *ApJ*, 678, 751  
 Rybicki, G. B. & Lightman, A. P., *Radiative Processes in Astrophysics*, 1979 John Wiley & Sons, New York, p146  
 Shemmer, O. et al. 2006, *ApJ*, 646, L29  
 Smith, K., L. et al. 2009, arXiv:0908.1998  
 Tremonti, C. et al. 2004, *ApJ*, 613, 898  
 Wang, J.-M., Watarai, K. & Mineshige, S. 2004, *ApJ*, 607, L107  
 Whittle, M. 1985a, *MNRAS*, 213, 1  
 Whittle, M. 1985b, *MNRAS*, 213, 33  
 Whittle, M. 1985c, *MNRAS*, 216, 817  
 Xu, D. et al. 2009, arXiv:0908.3140  
 Yang, F. et al. 2007, *ChJA&A*, 7, 353  
 Zhou, H. et al. 2004, *ApJ*, 604, L33

TABLE 1  
THE SAMPLE OF 87 TYPE 2 AGNs

Name (1)	$z$ (2)	$\Delta\lambda_1$ (3)	$\Delta\lambda_2$ (4)	$F_{[\text{O III}]1}$ (5)	$F_{[\text{O III}]2}$ (6)	$\mathcal{D}$ (7)
SDSS J000249+004504	$0.08662 \pm 5 \times 10^{-5}$	$5.18 \pm 0.07$	$3.76 \pm 0.05$	$662 \pm 13$	$731 \pm 13$	0.13
SDSS J000656+154847	$0.12515 \pm 2 \times 10^{-5}$	$3.30 \pm 0.10$	$3.14 \pm 0.09$	$618 \pm 19$	$498 \pm 19$	0.10
SDSS J013555+143529	$0.07208 \pm 2 \times 10^{-5}$	$2.35 \pm 0.08$	$2.30 \pm 0.05$	$586 \pm 17$	$328 \pm 15$	0.14
SDSS J014209-005049	$0.13253 \pm 2 \times 10^{-5}$	$1.20 \pm 0.12$	$2.94 \pm 0.17$	$360 \pm 28$	$377 \pm 28$	—
SDSS J015605-000721	$0.08084 \pm 2 \times 10^{-5}$	$2.77 \pm 0.08$	$2.67 \pm 0.10$	$545 \pm 18$	$427 \pm 18$	—
SDSS J073509+403624	$0.10297 \pm 2 \times 10^{-5}$	$1.99 \pm 0.11$	$2.35 \pm 0.04$	$686 \pm 25$	$640 \pm 24$	—
SDSS J074729+344018	$0.12982 \pm 2 \times 10^{-5}$	$3.27 \pm 0.10$	$2.11 \pm 0.13$	$57 \pm 4$	$69 \pm 4$	—
SDSS J074953+451454	$0.03132 \pm 1 \times 10^{-5}$	$1.97 \pm 0.09$	$2.35 \pm 0.07$	$746 \pm 31$	$796 \pm 31$	—
SDSS J075223+273643	$0.06908 \pm 2 \times 10^{-5}$	$2.24 \pm 0.05$	$2.42 \pm 0.03$	$747 \pm 16$	$980 \pm 16$	0.03
SDSS J080218+304622	$0.07654 \pm 3 \times 10^{-5}$	$2.99 \pm 0.04$	$3.02 \pm 0.04$	$2002 \pm 31$	$2575 \pm 32$	0.02
SDSS J080418+305157	$0.14553 \pm 2 \times 10^{-5}$	$3.25 \pm 0.06$	$4.83 \pm 0.03$	$210 \pm 4$	$198 \pm 4$	0.61
SDSS J080740+390015	$0.02346 \pm 1 \times 10^{-5}$	$5.44 \pm 0.06$	$4.72 \pm 0.07$	$1762 \pm 26$	$1529 \pm 25$	—
SDSS J080841+481351	$0.12365 \pm 4 \times 10^{-5}$	$4.82 \pm 0.16$	$1.85 \pm 0.12$	$414 \pm 23$	$654 \pm 23$	0.18
SDSS J081430+265729	$0.07874 \pm 4 \times 10^{-5}$	$3.04 \pm 0.06$	$2.22 \pm 0.06$	$430 \pm 15$	$593 \pm 16$	0.09
SDSS J082107+502115	$0.09534 \pm 3 \times 10^{-5}$	$2.85 \pm 0.16$	$2.85 \pm 0.09$	$281 \pm 15$	$312 \pm 14$	—
SDSS J085416+502631	$0.09553 \pm 4 \times 10^{-5}$	$2.32 \pm 0.04$	$3.16 \pm 0.03$	$502 \pm 9$	$520 \pm 9$	0.25
SDSS J085512+642345	$0.03621 \pm 1 \times 10^{-5}$	$2.52 \pm 0.07$	$2.26 \pm 0.06$	$372 \pm 11$	$338 \pm 11$	—
SDSS J085841+104122	$0.14810 \pm 5 \times 10^{-5}$	$3.31 \pm 0.05$	$3.25 \pm 0.04$	$863 \pm 11$	$653 \pm 11$	0.69
SDSS J094124+394441	$0.10750 \pm 3 \times 10^{-5}$	$2.68 \pm 0.08$	$2.10 \pm 0.07$	$774 \pm 32$	$1218 \pm 33$	0.29
SDSS J094427+144717	$0.07744 \pm 2 \times 10^{-5}$	$4.59 \pm 0.12$	$1.86 \pm 0.09$	$66 \pm 5$	$194 \pm 6$	—
SDSS J095528+383827	$0.06124 \pm 2 \times 10^{-5}$	$3.38 \pm 0.14$	$4.45 \pm 0.20$	$309 \pm 14$	$252 \pm 12$	0.70
SDSS J095833-005118	$0.08587 \pm 3 \times 10^{-5}$	$3.23 \pm 0.08$	$3.56 \pm 0.05$	$674 \pm 17$	$785 \pm 17$	0.23
SDSS J101143+325943	$0.12974 \pm 4 \times 10^{-5}$	$2.71 \pm 0.02$	$3.26 \pm 0.02$	$974 \pm 10$	$1220 \pm 11$	0.03
SDSS J101346-005451	$0.04243 \pm 2 \times 10^{-5}$	$4.57 \pm 0.12$	$3.02 \pm 0.08$	$359 \pm 10$	$574 \pm 11$	—
SDSS J101348+002014	$0.11711 \pm 3 \times 10^{-5}$	$2.39 \pm 0.33$	$3.08 \pm 0.14$	$156 \pm 17$	$178 \pm 16$	—
SDSS J102325+324348	$0.12701 \pm 5 \times 10^{-5}$	$3.04 \pm 0.20$	$3.41 \pm 0.15$	$189 \pm 14$	$244 \pm 14$	0.39
SDSS J104813+442710	$0.13972 \pm 3 \times 10^{-5}$	$3.13 \pm 0.27$	$2.47 \pm 0.14$	$51 \pm 6$	$80 \pm 6$	—
SDSS J105653+331945	$0.05104 \pm 2 \times 10^{-5}$	$3.75 \pm 0.04$	$5.38 \pm 0.07$	$944 \pm 11$	$553 \pm 9$	—
SDSS J110215+290725	$0.10603 \pm 3 \times 10^{-5}$	$3.08 \pm 0.13$	$4.22 \pm 0.11$	$295 \pm 12$	$229 \pm 11$	0.04
SDSS J110821+591851	$0.08572 \pm 2 \times 10^{-5}$	$2.48 \pm 0.05$	$2.49 \pm 0.05$	$919 \pm 21$	$968 \pm 21$	0.04
SDSS J110832+195128	$0.10317 \pm 3 \times 10^{-5}$	$3.54 \pm 0.22$	$3.19 \pm 0.12$	$325 \pm 26$	$692 \pm 27$	0.27
SDSS J110957+020138	$0.06322 \pm 2 \times 10^{-5}$	$3.06 \pm 0.07$	$2.85 \pm 0.03$	$723 \pm 21$	$1863 \pm 26$	0.17
SDSS J111042+030033	$0.10752 \pm 4 \times 10^{-5}$	$2.18 \pm 0.08$	$3.46 \pm 0.09$	$302 \pm 11$	$356 \pm 11$	0.47
SDSS J111054+012936	$0.12946 \pm 4 \times 10^{-5}$	$1.52 \pm 0.08$	$2.37 \pm 0.06$	$526 \pm 22$	$633 \pm 22$	—
SDSS J111201+275053	$0.04743 \pm 2 \times 10^{-5}$	$3.85 \pm 0.18$	$2.18 \pm 0.12$	$229 \pm 18$	$435 \pm 19$	0.45
SDSS J111333+165711	$0.05343 \pm 2 \times 10^{-5}$	$1.68 \pm 0.12$	$4.46 \pm 0.04$	$293 \pm 8$	$380 \pm 9$	0.41
SDSS J111803+062657	$0.12781 \pm 2 \times 10^{-5}$	$2.73 \pm 0.15$	$3.72 \pm 0.14$	$311 \pm 16$	$298 \pm 16$	0.50
SDSS J112659+294442	$0.10180 \pm 3 \times 10^{-5}$	$2.11 \pm 0.03$	$3.18 \pm 0.04$	$843 \pm 12$	$680 \pm 12$	0.24
SDSS J113126-020459	$0.14641 \pm 5 \times 10^{-5}$	$4.04 \pm 0.05$	$2.66 \pm 0.06$	$452 \pm 9$	$320 \pm 8$	—
SDSS J113630+135848	$0.08173 \pm 3 \times 10^{-5}$	$3.05 \pm 0.18$	$1.07 \pm 0.15$	$74 \pm 11$	$190 \pm 12$	—
SDSS J113759+143733	$0.08103 \pm 2 \times 10^{-5}$	$2.74 \pm 0.14$	$2.54 \pm 0.11$	$270 \pm 18$	$401 \pm 18$	—
SDSS J114047+445208	$0.06917 \pm 2 \times 10^{-5}$	$5.00 \pm 0.10$	$1.91 \pm 0.20$	$118 \pm 6$	$149 \pm 7$	—
SDSS J114249+102700	$0.11870 \pm 4 \times 10^{-5}$	$3.15 \pm 0.24$	$3.58 \pm 0.09$	$110 \pm 6$	$136 \pm 6$	—
SDSS J114610-022619	$0.12251 \pm 4 \times 10^{-5}$	$2.23 \pm 0.04$	$1.95 \pm 0.06$	$348 \pm 10$	$421 \pm 10$	—
SDSS J114840-021637	$0.08481 \pm 3 \times 10^{-5}$	$3.21 \pm 0.05$	$2.97 \pm 0.07$	$406 \pm 11$	$491 \pm 12$	0.28
SDSS J115028+044141	$0.04037 \pm 1 \times 10^{-5}$	$2.74 \pm 0.08$	$2.55 \pm 0.04$	$1128 \pm 36$	$2300 \pm 39$	0.05
SDSS J115249+190300	$0.09666 \pm 4 \times 10^{-5}$	$2.25 \pm 0.12$	$3.12 \pm 0.05$	$700 \pm 23$	$561 \pm 22$	—
SDSS J115548+110159	$0.10506 \pm 5 \times 10^{-5}$	$3.21 \pm 0.23$	$1.70 \pm 0.29$	$83 \pm 11$	$86 \pm 11$	—
SDSS J120320+131931	$0.05844 \pm 2 \times 10^{-5}$	$2.57 \pm 0.14$	$2.37 \pm 0.13$	$172 \pm 13$	$193 \pm 13$	—
SDSS J120357+280856	$0.06934 \pm 2 \times 10^{-5}$	$2.21 \pm 0.10$	$2.40 \pm 0.11$	$208 \pm 10$	$140 \pm 9$	0.89
SDSS J120802+230430	$0.07363 \pm 3 \times 10^{-5}$	$2.41 \pm 0.09$	$2.76 \pm 0.12$	$263 \pm 11$	$188 \pm 11$	0.03
SDSS J121311+650818	$0.13541 \pm 4 \times 10^{-5}$	$1.84 \pm 0.14$	$2.79 \pm 0.05$	$54 \pm 4$	$177 \pm 5$	0.06
SDSS J121527+000109	$0.10033 \pm 3 \times 10^{-5}$	$2.12 \pm 0.42$	$1.78 \pm 0.42$	$196 \pm 49$	$244 \pm 49$	—
SDSS J123524+060810	$0.09413 \pm 2 \times 10^{-5}$	$3.13 \pm 0.12$	$2.57 \pm 0.07$	$270 \pm 13$	$425 \pm 13$	—
SDSS J123538+050221	$0.06532 \pm 2 \times 10^{-5}$	$2.01 \pm 0.29$	$2.36 \pm 0.13$	$65 \pm 9$	$88 \pm 9$	—
SDSS J125049+074618	$0.05038 \pm 2 \times 10^{-5}$	$1.52 \pm 0.08$	$2.19 \pm 0.09$	$195 \pm 10$	$144 \pm 9$	—
SDSS J131235+500415	$0.11586 \pm 3 \times 10^{-5}$	$2.79 \pm 0.19$	$3.72 \pm 0.22$	$198 \pm 17$	$87 \pm 12$	—
SDSS J131515+213403	$0.07028 \pm 3 \times 10^{-5}$	$4.58 \pm 0.08$	$2.16 \pm 0.05$	$863 \pm 22$	$1364 \pm 23$	0.27
SDSS J132547+545019	$0.14183 \pm 4 \times 10^{-5}$	$1.76 \pm 0.12$	$2.76 \pm 0.16$	$396 \pm 27$	$412 \pm 27$	—
SDSS J133723+035350	$0.02280 \pm 1 \times 10^{-5}$	$2.42 \pm 0.08$	$2.75 \pm 0.16$	$514 \pm 23$	$272 \pm 22$	0.03
SDSS J133804+264209	$0.10667 \pm 2 \times 10^{-5}$	$1.92 \pm 0.56$	$1.83 \pm 0.40$	$67 \pm 18$	$55 \pm 18$	—
SDSS J135207+052555	$0.07883 \pm 2 \times 10^{-5}$	$2.14 \pm 0.15$	$3.15 \pm 0.05$	$714 \pm 33$	$952 \pm 32$	0.01
SDSS J142039+495906	$0.06333 \pm 2 \times 10^{-5}$	$2.74 \pm 0.19$	$1.80 \pm 0.10$	$165 \pm 16$	$318 \pm 17$	—
SDSS J143132+435807	$0.09604 \pm 4 \times 10^{-5}$	$2.89 \pm 0.33$	$3.23 \pm 0.35$	$60 \pm 9$	$66 \pm 9$	—
SDSS J143434+140548	$0.06974 \pm 3 \times 10^{-5}$	$1.99 \pm 0.36$	$3.21 \pm 0.44$	$140 \pm 22$	$119 \pm 22$	—

TABLE 1— *Continued*

Name (1)	$z$ (2)	$\Delta\lambda_1$ (3)	$\Delta\lambda_2$ (4)	$F_{[\text{O III}]1}$ (5)	$F_{[\text{O III}]2}$ (6)	$\mathcal{D}$ (7)
SDSS J145217+511050	$0.07582 \pm 3 \times 10^{-5}$	$2.08 \pm 0.17$	$3.79 \pm 0.12$	$500 \pm 25$	$379 \pm 24$	—
SDSS J145801+274251	$0.11845 \pm 3 \times 10^{-5}$	$2.79 \pm 0.23$	$2.61 \pm 0.26$	$207 \pm 20$	$201 \pm 21$	—
SDSS J150053+382349	$0.14523 \pm 5 \times 10^{-5}$	$3.10 \pm 0.08$	$2.59 \pm 0.09$	$475 \pm 15$	$452 \pm 15$	0.34
SDSS J150452+321414	$0.11253 \pm 4 \times 10^{-5}$	$1.86 \pm 0.21$	$2.38 \pm 0.12$	$194 \pm 21$	$277 \pm 25$	—
SDSS J151659+051751	$0.05122 \pm 1 \times 10^{-5}$	$2.10 \pm 0.04$	$3.31 \pm 0.03$	$685 \pm 11$	$729 \pm 12$	0.36
SDSS J151709+335324	$0.13541 \pm 6 \times 10^{-5}$	$6.75 \pm 0.01$	$5.57 \pm 0.02$	$3659 \pm 16$	$2232 \pm 11$	—
SDSS J152606+414014	$0.00831 \pm 0.7 \times 10^{-5}$	$2.92 \pm 0.04$	$1.83 \pm 0.05$	$3146 \pm 96$	$6776 \pm 105$	0.15
SDSS J153217+453225	$0.07138 \pm 3 \times 10^{-5}$	$2.71 \pm 0.12$	$1.58 \pm 0.07$	$170 \pm 11$	$261 \pm 11$	0.14
SDSS J153315+575001	$0.06734 \pm 2 \times 10^{-5}$	$3.08 \pm 0.06$	$2.37 \pm 0.09$	$337 \pm 11$	$311 \pm 11$	—
SDSS J155205+043317	$0.08016 \pm 3 \times 10^{-5}$	$2.78 \pm 0.09$	$2.14 \pm 0.05$	$112 \pm 6$	$298 \pm 6$	—
SDSS J155619+094855	$0.06785 \pm 1 \times 10^{-5}$	$3.12 \pm 0.04$	$3.65 \pm 0.02$	$783 \pm 10$	$1112 \pm 10$	0.11
SDSS J160024+264035	$0.09003 \pm 4 \times 10^{-5}$	$3.94 \pm 0.36$	$3.48 \pm 0.26$	$88 \pm 12$	$153 \pm 13$	0.11
SDSS J160436+500958	$0.14649 \pm 3 \times 10^{-5}$	$2.94 \pm 0.04$	$3.22 \pm 0.05$	$353 \pm 7$	$354 \pm 7$	0.08
SDSS J160524+152233	$0.04210 \pm 1 \times 10^{-5}$	$3.23 \pm 0.18$	$2.81 \pm 0.12$	$200 \pm 17$	$386 \pm 17$	0.37
SDSS J160636+342754	$0.05473 \pm 2 \times 10^{-5}$	$2.70 \pm 0.20$	$1.94 \pm 0.17$	$230 \pm 23$	$288 \pm 23$	—
SDSS J161006+210735	$0.13722 \pm 2 \times 10^{-5}$	$3.49 \pm 0.05$	$2.01 \pm 0.03$	$170 \pm 5$	$486 \pm 6$	0.21
SDSS J162939+240856	$0.05921 \pm 2 \times 10^{-5}$	$2.60 \pm 0.13$	$1.69 \pm 0.13$	$133 \pm 10$	$115 \pm 9$	—
SDSS J163316+262716	$0.07125 \pm 4 \times 10^{-5}$	$2.10 \pm 0.21$	$3.11 \pm 0.29$	$160 \pm 15$	$105 \pm 15$	—
SDSS J165206+310707	$0.07495 \pm 2 \times 10^{-5}$	$2.04 \pm 0.08$	$3.15 \pm 0.07$	$115 \pm 5$	$157 \pm 5$	0.09
SDSS J225420-005134	$0.07950 \pm 3 \times 10^{-5}$	$3.17 \pm 0.11$	$3.78 \pm 0.12$	$183 \pm 8$	$112 \pm 7$	0.15
SDSS J230442-093345	$0.03203 \pm 1 \times 10^{-5}$	$2.69 \pm 0.10$	$2.67 \pm 0.17$	$449 \pm 24$	$393 \pm 25$	—
SDSS J231051-090011	$0.09439 \pm 2 \times 10^{-5}$	$1.20 \pm 0.03$	$4.28 \pm 0.03$	$640 \pm 8$	$428 \pm 7$	0.20

NOTE: Col (1): SDSS names of objects; Col (2) redshifts and their uncertainties; Col. (3) and (4) are the Doppler red and blue shifts of [O III] line in units of  $\text{\AA}$ , respectively.; Col (5) and (6) are the corresponding fluxes in units of  $10^{-17} \text{ergs s}^{-1} \text{cm}^{-2}$ , respectively. (7) parameter  $\mathcal{D}$  is the separation of the two components in the BPT diagram.

This is only part of the full table. See the complete sample online.